INORGANIC CHEMISTRY
FRONTIERS

CHINESE CHEMICAL SOCIETY

ROYAL SOCIETY OF CHEMISTRY

RESEARCH ARTICLE

View Article Online
View Journal | View Issue

Cite this: *Inorg. Chem. Front.*, 2022, **9**, 2617

Achieving ultra-dispersed 1T-Co-MoS_2@HMCS *via* space-confined engineering for highly efficient hydrogen evolution in the universal pH range†

Changle Yue,[a] Yan Zhou, [b] Yang Liu,[a] Chao Feng,[a] Wenjing Bao,[a] Fengyue Sun,[a] Yongxiao Tuo,[b] Yuan Pan, [a] Yunqi Liu[a] and Yukun Lu *[a]

Received 4th February 2022,
Accepted 11th April 2022

DOI: 10.1039/d2qi00269h

rsc.li/frontiers-inorganic

The rational design and synthesis of noble-metal-free electrocatalysts for water splitting is always important for the future hydrogen economy. Therefore, it is necessary to design an effective transition metal sulfide down to a molecular level. In this work, a multi-level spatial confinement strategy was developed to fabricate Co-promoted 1T-MoS_2 (1T-Co-MoS_2) by employing Evans–Showell-type polyoxometalates (POMs) $[Co_2Mo_{10}O_{38}H_4]$ as molecular precursor. Highly dispersed 1T-Co-MoS_2 nanoclusters with few layers (1–3 layers) and ultrasmall size (<5 nm) were synthesized within the hollow mesoporous carbon sphere (HMCS) by *in situ* vapor phase sulfurization. During the preparation, coordination bonds, organic cations and mesopores provide a triple-confinement environment to limit the growth of 1T-Co-MoS_2 from the atomic level, molecular level to mesoscopic scale. The obtained 1T-Co-MoS_2@HMCS exhibits remarkable electrocatalytic activity and excellent long-term durability for hydrogen evolution reaction (HER), with overpotentials of 220 and 245 mV to achieve the current density of 200 mA cm^{-2} in 1 M KOH and 0.5 M H_2SO_4, respectively. The corresponding theoretical calculations indicate that Co–S edge sites are the most active sites of 1T-Co-MoS_2 for HER, reflecting the major significance of Co doping. The superior HER performance could be attributed to the high intrinsic activity from Co-doped 1T-MoS_2 sites, abundant exposed active sites from ultra-dispersed nanosheets, and enhanced charge and mass transfer within the HMCS substrate. This work provides a novel design concept *via* hierarchical multiple-level confinement for the synthesis of high-quality 1T-Co-MoS_2 and achieves outstanding performance in electrocatalytic HER.

1. Introduction

Hydrogen energy is one of the effective solutions for the current increasing energy demand and environmental pollution caused by fossil energy.[1] In recent years, electrocatalytic water splitting to generate stable and sustainable clean hydrogen fuels has attracted considerable attention.[2] Although noble-metal-based hydrogen evolution reaction (HER) catalysts show high activity, their practical applications are limited by their high cost and low abundance.[3] Therefore, it is urgent to explore earth-abundant electrocatalysts for electrocatalytic water splitting with high efficiency and stability.[4] A large variety of non-noble metal catalysts including metal phosphides,[5] carbides,[6] and dichalcogenides[7,8] have been explored to replace noble-metal-based electrocatalysts. Among them, two-dimensional (2D) molybdenum disulfide (MoS_2) is one of the most investigated electrocatalysts for the HER process.[7,9] MoS_2 has attracted much attention in the field of hydrogen production due to its similar Gibbs free energy (ΔG_{H^*}) for hydrogen absorption to that of Pt and its flexible molecular structure.[10] The S-edge sites of MoS_2 are thermally neutral to hydrogen absorption (ΔG_{H^*} = 0.08 eV) and are considered to be the catalytic active centers.[11] Among the different crystalline phases of MoS_2, 1T-MoS_2 is a metallic phase with an electrical conductivity 10^7 times higher than that of 2H-MoS_2, which can greatly improve the charge transfer efficiency in the HER process.[12] It was demonstrated that both the basal planes and edges of the 1T phase are active sites for HER, which leads to excellent electrocatalytic activity.[13] In particular, 1T-MoS_2 shows more efficient HER activity than that of 2H-MoS_2 in acidic solutions due to the partially filled Mo 4d and S 3p electronic states around the Fermi level.[14] Although 1T-MoS_2

---

[a] *State Key Laboratory of Heavy Oil Processing, College of Chemistry and Chemical Engineering, China University of Petroleum (East China), Qingdao 266580, PR China. E-mail: lyk@upc.edu.cn*

[b] *School of Materials Science and Engineering, China University of Petroleum (East China), Qingdao 266580, PR China*

† Electronic supplementary information (ESI) available. See DOI: **https://doi.org/10.1039/d2qi00269h**

offers more active sites and adequate H adsorption, its catalytic performance of HER in alkaline solutions still needs to be improved.[15] The slow HER kinetics of 1T-MoS_2 in alkaline solutions is due to the rather sluggish initial water splitting step (Volmer step).[16]

Heteroatom doping strategy has been widely applied to MoS_2 to further enhance its HER catalytic activity by further tuning its electronic structure.[17,18] Grønborg[19] *et al.* has demonstrated that the MoS_2 cluster can be doped by Co to provide both Mo- and S-terminated edges when the MoS_2 cluster size is larger than ~2 nm. Because the thermodynamic stability of 1T phase is less than that of 2H phase of MoS_2, 1T-MoS_2 can only be obtained under harsh synthetic strategies.[12,20] Although extensive research has been carried out to seek the way of fabricating heteroatom-doped 1T-MoS_2, it is rather complicated to obtain single 1T phase MoS_2 by a conventional hydrothermal (or solvothermal) method.[21–23] Thus, it is difficult to synthesize heteroatom-doped 1T-MoS_2 on a large scale. However, it has been found that metastable 1T-MoS_2 can be achieved by confining the lateral size and stacking numbers of MoS_2 nanosheets.[24] Thus, it is reasonable to believe that a confinement approach can lead to successful synthesis of heteroatom-doped 1T-MoS_2 when its size can be confined to less than ~5 nm in diameter and the stacking numbers can be reduced to single or few layers.

Recently, polyoxometalates (POMs) display great advantages as an excellent bimetallic precursor platform.[6,7,25–28] It provides more than one type of transition metal element in a single-molecular level. Owing to the sub-nanometer size, well-defined structure, and tunable chemical composition, Mo-containing POMs have been widely studied as molecular-level precursors to fabricate a Mo-based active phase with a relatively uniform size and homogeneous structure.[24,29] Our previous investigations also showed that the use of Co_5Mo_{10} as a precursor can successfully obtain ultra-small-sized MoS_2 and CoS.[25] Single-phase Co-doped 1T-MoS_2 was not achieved in the previous investigation because of the rather rigorous sulfidation conditions and the aggregation of the precursors during the sulfidation process. Thankfully, we have discovered a multi-level confinement strategy to achieve ultra-small single-phase Co-doped 1T-MoS_2 by ion exchange and vapor phase sulfidation in mesopores with POMs. The cations of POMs can be easily exchanged by cationic surfactants, and thus, they can interconnect the POMs and anchor each POM unit in specific positions up to a supramolecular level. However, supramolecules are more likely to grow into large MoS_2 nanosheets or nano-blocks during sulfidation, which is not conducive to the synthesis of small-sized 1T-MoS_2.[30] Therefore, further spatial confinement, an excellent way to induce the 2D nanosheet with metastable phases, is needed to limit the growth of catalytic materials.[23,31] HMCS have been previously reported as typical synthetic nanoreactors, which illustrated their competitive potential in heterogeneous catalysis due to their adjustable microenvironmental effects.[32] The mesoporous confinement effect of HMCS proves to be the key to improving catalytic performance, and it is essentially driven by an integrated action of electronic metal–support interaction, reactant enrichment and diffusion, which are mainly ascribed to the peculiar properties of hollow nanoreactors in both electronic and structural aspects, respectively.[33,34] Accordingly, multiple confinement strategies at different scales can be integrated to prepare highly dispersed heteroatom-doped 1T-MoS_2.

As illustrated in Fig. 1, the bottom-up multi-level spatial confinement strategy is presented for the design and fabrication of ultra-dispersed 1T-Co-MoS_2 nanoclusters employing Evans–Showell-type POMs $(NH_4)_6[Co_2Mo_{10}O_{38}H_4]$ (denoted as Co_2Mo_{10}) as precursors. The multiple confined processes are achieved by rationally utilizing hierarchical interactions from the atomic level to the mesoscopic scale: (1) Chemical bond confinement at the atomic level, in which the Co atoms are anchored *via* Co–O–Mo coordinative bonding and encapsulated within single POM clusters possessing a stable and specific Co_2Mo_{10} structure, which realizes the close contact of Mo and Co atoms and guarantees enormously the catalytic synergism of binary Co-doped MoS_2 active sites for HER. (2) Organic cation confinement at the molecular level, which is achieved by selecting hexamethonium (HM) bromide as the appropriate counter-cation, with single $[Co_2Mo_{10}]^{6-}$ polyoxoanion spontaneously separated and integrated into inorganic–organic hybrid networks $(Co_2Mo_{10})(HM)_3$ *via* electrovalent bonding, thereby deriving superior dispersed Co-doped MoS_2 nanosheets with few layers. (3) Mesopore confinement at nanoscale, in which the HMCS provides abundant pore structures, with soluble $(Co_2Mo_{10})(HM)_3$ hybrid molecules that were adsorbed and spatially confined within nanosized meso-cages, and then homogeneously distributed throughout conductive H substrates, effectively inhibiting the agglomeration and migration during the following sulfurization, and maintaining the ultrafine Co-MoS_2 nanosheets inside the nano-space. As we expected, the obtained 1T-Co-MoS_2@HMCS possesses the aforementioned structural superiorities and exhibits remarkable electrocatalytic activities and excellent long-term durability towards HER in both alkaline and acidic electrolytes. Thus, this work provides a novel design concept *via* hierarchical multi-level confinement for the synthesis of high-quality 1T-Co-MoS_2 to enhance the electrocatalytic performance.

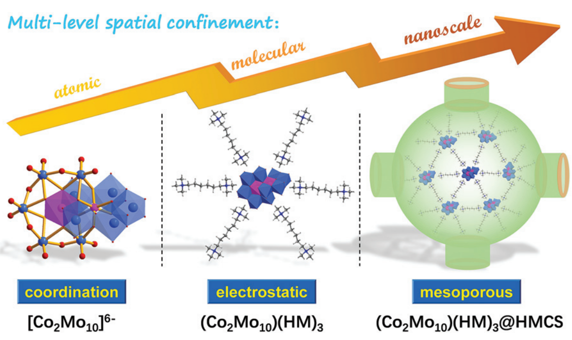

Fig. 1 Schematic diagram of the preparation of $(Co_2Mo_{10})(HM)_3$@HMCS precursors by a multi-level confined strategy.

2. Experimental section

All the chemicals used in this study were purchased and used without further purification.

2.1 Preparation of HMCS

First, 7.00 mL $NH_3 \cdot H_2O$ was added to 160 mL aqueous solution of ethanol ($V_{ethanol} : V_{water}$ = 7 : 1) to obtain an alkaline environment. After sufficient magnetic stirring, 7.00 mL TPOS (24.2 mmol) was added slowly to the solution and stirred for 30 min. Then, 1.12 mL CH_2O (13.8 mmol) solution and 0.800 g $C_6H_6O_2$ (7.27 mmol) dissolved in 4.00 mL ethanol by ultrasonication were slowly dropped into the above solution. After stirring for 24 h at room temperature, light yellow SiO_2 precipitates were separated from the creamy white solution by centrifugation and dried at 60 °C. The SiO_2 powder was then carbonized at 900 °C for 4 h in a N_2 (99.999%) atmosphere at a heating rate of 5 °C min^{-1}, followed by natural cooling to produce black SiO_2@C spheres. The black HMCS powder could be obtained by SiO_2@C spheres stirred in a 13 wt% HF solution for 2 days.

2.2 Preparation of $(NH_4)6[Co_2Mo_{10}H_4O_{38}] \cdot 4H_2O$ (Co_2Mo_{10})

Ammonium salt of decamolybdodicobaltate Co_2Mo_{10} was synthesized according to the published procedure.[28] First, 15.0 g (12.1 mmol) $(NH_4)_6Mo_7O_{24} \cdot 4H_2O$ and 3.10 g (12.4 mmol) Co $(CH_3COO)_2 \cdot 4H_2O$ were dissolved in 125 mL water, and then 3.00 g active charcoal and 20.0 mL peroxide solution (18%) were added to the solution. After boiling the black solution for 1 h, the active charcoal was separated by filtration. Dark-green Co_2Mo_{10} crystals were obtained by slow evaporation of the solvent at room temperature.

2.3 Synthesis of $(Co_2Mo_{10})(HM)_3$@HMCS

Co_2Mo_{10} was used as the source for both Co and Mo. First, 0.248 g (0.133 mmol) Co_2Mo_{10} and 0.144 g (0.399 mmol) hexamethonium (HM) bromide were dissolved in 20.0 mL deionized water. Then, 30.0 mg HMCS was added to the clear green solution and stirred at room temperature for 12 h to obtain $(Co_2Mo_{10})(HM)_3$@HMCS. The black (Co_2Mo_{10}) $(HM)_3$@HMCS precipitates were separated by centrifugation, washed several times with deionized water and dried at 60 °C for 24 h.

2.4 Synthesis of 1T-Co-MoS_2@HMCS

In this work, 1T-Co-MoS_2@HMCS was obtained by calcining $(Co_2Mo_{10})(HM)_3$@HMCS under 10 vol% H_2S/H_2 at 400 °C for 4 h at a heating rate of 5 °C min^{-1}.

2.5 Synthesis of Co-MoS_2@HMCS

Co-MoS_2@HMCS was obtained without HM compared with 1T-Co-MoS_2@HMCS. First, 0.248 g (0.133 mmol) Co_2Mo_{10} was dissolved in 20 mL deionized water for 30 min. Then, 30.0 mg HMCS was added to this solution and stirred for 12 h. The as-synthesized black product was separated by centrifugation, washed several times with deionized water and then dried at 60 °C for 24 h. Then, the prepared sample was further calcined under 10 vol% H_2S/H_2 at 400 °C for 4 h at a heating rate of 5 °C min^{-1}, followed by natural cooling to produce Co-MoS_2@HMCS powder.

2.6 Synthesis of Co-MoS_2

Co-MoS_2 was prepared by calcining Co_2Mo_{10} at 400 °C for 4 h at a heating rate of 5 °C min^{-1} in a 10 vol% H_2S/H_2 atmosphere.

2.7 Synthesis of MoS_2@HMCS and CoS@HMCS

First, 0.282 g (0.228 mmol) $(NH_4)_6Mo_7O_{24} \cdot 4H_2O$ or 0.398 g (1.60 mmol) $Co(CH_3COO)_2 \cdot 4H_2O$ was dissolved in 20.0 mL deionized water containing 0.144 g (0.399 mmol) hexamethonium (HM) bromide for 30 min. Then, 30.0 mg HMCS was added to this solution and stirred for 12 h. The as-synthesized product was separated by centrifugation, washed several times with deionized water and then dried at 60 °C for 24 h. Then, the prepared sample was further calcined under 10 vol% H_2S/H_2 at 400 °C for 4 h at a heating rate of 5 °C min^{-1}, followed by natural cooling to produce a MoS_2@HMCS or CoS@HMCS powder.

2.8 Synthesis of 2H-MoS_2

Hydrothermal synthesis in a sealed autoclave system was used for the preparation of 2H-MoS_2. First, 1.44 g (10 mmol) MoO_3 and 3.04 g (40 mmol) CH_4N_2S were dispersed in 70 mL deionized water under stirring to form a homogeneous solution. Then, the above solution was transferred into a 100 mL Teflon-lined stainless steel autoclave and kept at 220 °C for 12 h. The final product was washed several times with deionized water and dried at 60 °C.

2.9 Structural characterizations

X-ray powder diffraction (XRD) patterns of the products were acquired using an X-ray diffractometer (BRUKER D8 ADVANCE) with Cu Kα radiation (λ = 1.5418 Å, 40 kV, 40 mA) at room temperature. Scanning electron microscopic (SEM) images of the products were acquired using a field-emission SEM (JMS-7900F). High-resolution transmission electron microscopic (HRTEM) images, energy-dispersive X-ray spectroscopy (EDX) spectra and annular dark-field STEM images of the products were recorded using a HRTEM (JEM-2100F). Fourier transform infrared (FT-IR) spectra were recorded using a VERTEX 80 V FT-IR spectrometer. The chemical states of the sample were determined by X-ray photoelectron spectroscopy (XPS) using a Thermo VG ESCALAB250XI surface analysis system. N_2 adsorption–desorption isotherms were obtained using a Quantachrome Autosorb-1-MP analyzer at 77 K and the specific surface area was calculated automatically using a multipoint Brunauer–Emmett–Teller (BET) model. Raman spectra of the catalysts were recorded using a Senterra laser Raman spectrometer (λ = 532 nm) equipped with an optical microscope in the confocal mode.

2.10 Electrochemical characterizations

All of the electrochemical performance tests in 1.0 M KOH and 0.5 M H_2SO_4 electrolyte media were performed using a Gamry INTERFACE 1000 E, USA, using a saturated calomel electrode (SCE) electrode, a graphite rod, and as-prepared bimetal sulfide electrodes as the reference electrode, the counter electrode, and the working electrode, respectively. All polarization curves at 2 mV s^{-1} were iR compensated. The linear sweep voltammetry (LSV) measurements were recorded at a scan rate of 2 mV s^{-1}. The cyclic voltammetry (CV) measurements were carried out with different sweep rates between 40 and 200 mV s^{-1}. The long-term stability tests were performed by CV tests at a scan rate of 100 mV s^{-1}. The electrochemical impedance spectroscopy (EIS) tests were performed by ac impedance spectroscopy in the frequency range of 10° to 1 Hz. According to the Nernst equation $E_{\mathrm{RHE}} = E_{\mathrm{SCE}} + 0.059\ \mathrm{pH} + 0.254$, where E_{RHE} is the potential *vs.* a reversible hydrogen electrode, E_{SCE} is the potential *vs.* an SCE electrode, and pH is the pH value of the electrolyte.

The surface of the glassy carbon electrode (GCE, 3 mm diameter) was polished with 0.3 μm alumina slurries and sonicated with deionized water and ethanol. Then, the electrode was dried at 25 °C. To prepare modified electrodes, 5.0 mg of electrocatalyst was dispersed into 1.005 mL of Nafion solution [5.0 μL Nafion (5%) dissolved in 1.000 mL of ethanol] to give a homogeneous suspension upon bath sonication. Then, 20.0 μL of the suspension was dropped onto the GCE surface and the electrode was dried at 25 °C.

3. Results and discussion

3.1 Preparation and characterization of 1T-Co-MoS_2@HMCS

The detailed synthesis procedures of Co_2Mo_{10} and HMCS were described in the ESI.† Accordingly, 1T-Co-MoS_2@HMCS is achieved *via* three steps, as displayed in Fig. 2. First, SiO_2@C was selectively etched to remove the SiO_2 template to form a hollow carbon sphere with a mesoporous shell and radially aligned channels. The HMCS can then be served as a nanoreactor to accommodate highly dispersed Co_2Mo_{10} within the cationic surfactants HM^{2+} to obtain the $(Co_2Mo_{10})(HM)_3$@HMCS precursor. Subsequently, spatially confined 1T-Co-MoS_2 in HMCS (1T-Co-MoS_2@HMCS) was constructed by vapor phase sulfurization in a tubular furnace at 400 °C for 4 h under a H_2S/H_2 atmosphere. During this process, the 1T phase Co-MoS_2 was facilely derived from Co_2Mo_{10} precursors *via in situ* O–S exchange and then uniformly dispersed throughout the HMCS frameworks. Thus, the as-prepared 1T-Co-MoS_2@HMCS can provide a large number of Co-doped 1T-MoS_2 active sites and efficient electric conductivity to achieve high catalytic activity and stability towards HER catalysis.

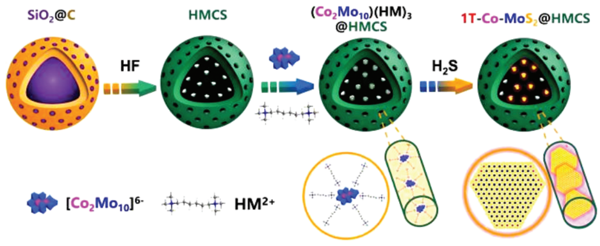

Fig. 2 Schematic illustration of the preparation approach of 1T-Co-MoS2@HMCS.

To further elucidate the spatial confinement effects provide by the surfactants and HMCS, XRD characterizations are applied to investigate the crystal structure of Co_2Mo_{10} and $(Co_2Mo_{10})(HM)_3$@HMCS. As shown in Fig. S1a,† the diffraction peaks of $(Co_2Mo_{10})(HM)_3$@HMCS shift to small angles, indicating that the crystal lattice of Co_2Mo_{10} is effectively enlarged by HM^{2+} organic chains under the action of spatial confined engineering, which provides a basis for ultra-dispersed catalysts. This suggests that the spatial confinement is effective on confining the POMs precursor, and thus, subsequently limits the growth of Co-MoS_2. Fig. S1b† represents the FT-IR results of Co_2Mo_{10} and $(Co_2Mo_{10})(HM)_3$@HMCS. The peaks at 615, 679, 863, 907, and 940 cm^{-1} are assigned to the stretching vibration of the Co–O, Mo–O–Mo, and Mo═O in Co_2Mo_{10} molecules. Besides, the peaks at 1405, 1615, and 3200–3600 cm^{-1} are ascribed to O–H and N–H modes in Co_2Mo_{10}, suggesting the existence of molecular water and NH_4^+. In comparison, the stretching vibration of Co–O, Mo–O–Mo, and Mo═O in $(Co_2Mo_{10})(HM)_3$@HMCS shifts toward a lower wave number, which could be attributed to the increased bond length caused by the enlarged lattice space.[35] At the same time, the FT-IR spectra of $(Co_2Mo_{10})(HM)_3$@HMCS do not contain peaks associated with O–H and N–H, indicating successful replacement of NH_4^+ cations on Co_2Mo_{10} by HM^{2+} cationic surfactants. The successful preparation of host–guest precursors $(Co_2Mo_{10})(HM)_3$@HMCS is attributed to the outstanding structure characteristics and self-assembly ability of $[Co_2Mo_{10}]^{6-}$ polyoxoanions.

Fig. 3a shows the SEM image of HMCS after the SiO_2 template was removed, with an average diameter of 450 ± 50 nm. The spherical structure of HMCS indicates that the removal process of SiO_2 did not affect the template morphology. The XRD and FT-IR characterizations shown in Fig. S2† suggest that SiO_2 was successfully removed by HF. After loading with $(Co_2Mo_{10})(HM)_3$ and followed by sulfidation, the spherical structure of HMCS is retained (Fig. 3b), suggesting the formation of Co-MoS_2 inside the pores of HMCS. The TEM image of broken spheres shown in Fig. 3c indicates the hollow structure of 1T-Co-MoS_2@HMCS, with the uniform size and a shell of ~50 nm thickness. To further understand the compositions within carbon spheres, XRD was applied. As shown in Fig. 3d, the characteristic diffraction peaks of MoS_2 are detected in 1T-Co-MoS_2@HMCS, and the distinct diffraction angle of the (002) crystal plane of MoS_2 significantly shifts to a lower angle (11.8°) compared to 14.4° of MoS_2 (PDF# 01–089–3040), due to the increase in MoS_2 interlayer spacing caused by the spatial confined effect. No other peaks related to Co species were

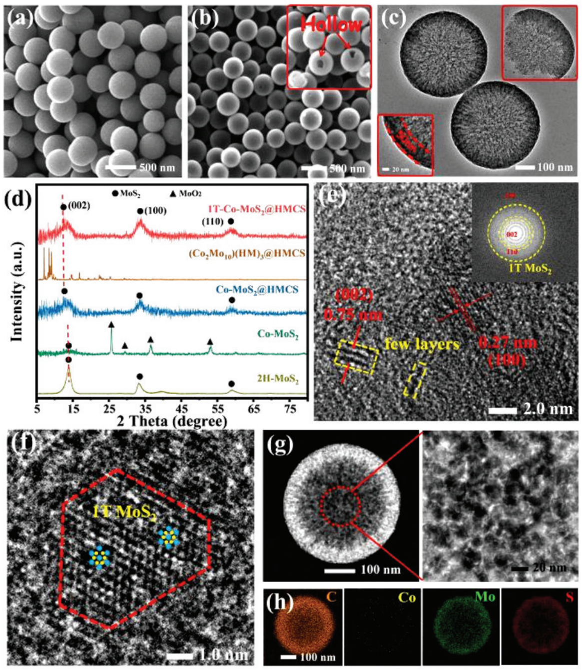

Fig. 3 (a and b) SEM images of HMCS and 1T-Co-MoS_2@HMCS, (c) TEM images of 1T-Co-MoS_2@HMCS, (d) XRD patterns for HMCS, Co-MoS_2, Co-MoS_2@HMCS, $(Co_2Mo_{10})(HM)_3$@HMCS and 1T-Co-MoS_2@HMCS, and (eand f) HRTEM images of 1T-Co-MoS_2@HMCS, (g) HAADF-STEM images, and (h) the EDX mapping obtained by TEM for selected area of 1T-Co-MoS_2@HMCS.

observed in the XRD patterns, suggesting that after a vapor phase sulfidation process, a single phase of Co-MoS_2 was successfully formed in the HMCS. Fig. 3e shows the HRTEM image and the corresponding FFT image (inset) of 1T-Co-MoS_2@HMCS, displays that the order lattice spacings are 0.75 and 0.27 nm, corresponding to the (002) and (100) crystal planes of MoS_2. This obvious increase in *d*-spacing in the (002) plane compared to conventional MoS_2 (0.62 nm) agrees with the findings from the XRD pattern and the calculated result from Bragg's equation.[7] The expanded interplanar spacing of MoS_2 can greatly favour the phase transition from 2H to 1T. Meanwhile, compared with Co-MoS_2 obtained by direct sulfidation of Co_2Mo_{10}, most of the MoO_2 phase remains, suggesting that the confined sulfidation process has a higher degree of sulfidation. The complete sulfidation of $(Co_2Mo_{10})(HM)_3$@HMCS is attributed to the higher degree of dispersion of Co_2Mo_{10} due to the confinement effects provided by HMCS and the cationic surfactants. This confirms that the HMCS provides a fine environment for MoS_2 to be formed and dispersed inside the carbon spheres due to the spatial confinement effect. In addition, compared to the XRD patterns of 1T-Co-MoS_2@HMCS, the materials obtained without addition of surfactant (Co-MoS_2@HMCS) show identical diffraction patterns, indicating that the HM^{2+} surfactant only serves as confinement agents during the sulfidation process and significantly improve the active phase dispersion (Fig. S3†).

Fig. 3f and Fig. S4† show the HRTEM images of 1T-Co-MoS_2 confined within HMCS. The ultra-small 1T-Co-MoS_2 cluster exhibits approximately truncated triangular shape, which is consistent with previous studies of the CoMoS phase.[19,36,37] According to the research of Lauritsen *et al.*,[19] this shape can indicate Co doping into a 1T-MoS_2 crystal lattice, where Co terminates the growth of 1T-MoS_2 along the (001) plane and promotes the formation of the Co-substituted S-edge. In other words, the modification to a partially truncated triangular shape was concluded to be driven by the preferential substitution of Co atoms at the S-edges, which further stabilizes the energy of the S-edge.[19] It was also demonstrated in similar research that CoMoS nanoparticles exhibit a truncated hexagonal equilibrium morphology due to Co deposition, exposing both Mo- and S-edges.[38] To the best of our knowledge, single-layer Co-MoS_2 was prepared with difficultly and observed in addition to the growth on the Au support by chemical vapor deposition. Furthermore, the lateral size of 1T-Co-MoS_2 was found to be ~4 nm, and the stacking number was observed in single or few layers (1–3 layers). The limited pore size and cationic surfactants could avoid the accumulation and growth of MoS_2 caused by sulfidation at the basal plane and epitaxial direction, respectively.[39] It is speculated that the appearance of Co-doped 1T-MoS_2 may originate from the large interlayer spacing with small size regulated by the spatially restricted domain and the electron-modulating effect of Co doping.[40,41] Thus, the truncated triangular morphology, few-layer stacking, and reduced lateral size observed in 1T-Co-MoS_2@HMCS could be attributed to the synergistically confined growth effect from the atomic level to the mesoscopic scale, which benefits from the hierarchical structural $(Co_2Mo_{10})(HM)_3$@HMCS precursor and *in situ* vapour-phase sulfurization approach.

The porous structures of HMCS on the shell of hollow nanospheres are further supported by the annular dark-field STEM analysis. As shown in Fig. 3g, the dark areas indicate the enrichment of mesopores in HMCS, and bright areas indicate the dispersion of Co-MoS_2 in the HMCS with small sizes. The elemental mappings from EDX show the presence and homogenous distribution of C, Co, Mo, and S (Fig. 3h), indicating that the synthetic method in this study implemented uniform dispersion of small-sized Co-MoS_2 in the HMCS nanoreactor and provided more discrete catalytic sites for HER. Meanwhile, it also benefits from the organic cation-confined engineering of Co–O–Mo within the POMs molecule, realizing doping and dispersion of the double transition metals at the molecular level. In addition, the BET analysis shows that the specific surface area of HMCS is about 1377 $m^2 g^{-1}$, and the main pore size is about 7.8 nm in diameter (Fig. S4†). The specific surface area of 1T-Co-MoS_2@HMCS is about 189.6 $m^2 g^{-1}$, and the main pore size is about 7.1 nm in diameter, which reveals the successful loading of MoS_2 nanosheets inside carbon spheres. These results show that the obtained 1T-Co-MoS_2@HMCS maintain the mesoporous structure of HMCS, which can expose the numerous 1T-Co-MoS_2 active sites and promote faster charge and mass transfer to enhance the electrocatalytic performance.

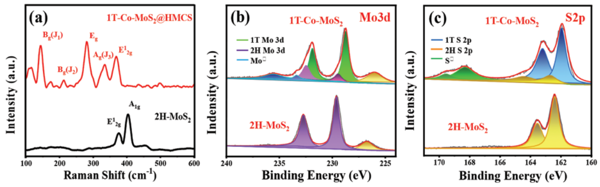

Fig. 4 (a) Raman spectra and high-resolution XPS spectra of (b) Mo 3d and (c) S 2p of 1T-Co-MoS_2@HMCS catalyst and 2H-MoS_2.

Raman spectra further confirm the existence of 1T-MoS_2 nanosheets in HMCS (Fig. 4a and S6†). The Raman spectrum of 1T-Co-MoS_2@HMCS reveals vibration peaks appearing at 144 (J_1), 235 (J_2), 283 (E_g), and 333 cm^{-1}(J_3), attributed to the highly distorted structure of 1T-MoS_2. The broadening of 404 (A_{1g}) and 375 cm^{-1} ($E^1{}_{2g}$) modes and the suppressed intensity of $E^1{}_{2g}$ are also typical for the 1T phase. To further demonstrate the high proportion of 1T-MoS_2, the Raman spectrum of pure 2H-MoS_2 is compared to 1T-Co-MoS_2@HMCS. Two strong fingerprint peaks of 2H-MoS_2 appear at 375 and 404 cm^{-1}, assigned to the in-plane and out-of-plane vibration modes of 2H-MoS_2, respectively. The comparison results show the high proportion of 1T-MoS_2 in 1T-Co-MoS_2@HMCS, which also coincides with the results of XPS. In addition, the three peaks between 800 and 1000 cm^{-1} are ascribed to the molecular structure of Mo_3S_{13},[42,43] which locate at the edge sites of MoS_2, thus further proving that the ultra-small nanosheets of 1T-Co-MoS_2@HMCS can expose a large quantity of under-coordinated Mo–S edge sites. The other two peaks located at 1341 and 1595 cm^{-1} in 1T-Co-MoS_2@HMCS are attributed to the D and G bands of graphitized carbon, which confirms the presence of the HMCS shell. Herein, it is confirmed by Raman spectroscopy that 1T-MoS_2 with abundant edge active sites loaded on carbon spheres was indeed prepared. To further verify the chemical composition and valence state of 1T-Co-MoS_2@HMCS, XPS analyses were carried out. Fig. S7a† shows the full XPS spectrum of 1T-Co-MoS_2@HMCS, indicating the existence of Co, N, C, Mo, and S. The results show a low atomic ratio of 0.65% Co, while the atomic ratio of Mo is 2.83%, which is about 5 times higher than that of Co. This coincides with the atomic ratio of POMs, Co_2Mo_{10}. In Fig. 4b, the peaks at around 229.0 and 232.2 eV correspond to the binding energies of Mo $3d_{3/2}$ and Mo $3d_{5/2}$ for 1T-MoS_2.[44] Compared to the deconvoluted peaks for 2H-MoS_2 (purple peaks), the decrease in the binding energy of 1T-MoS_2 is because the Mo–S bond in the unit cell has a shorter bond length than that of the 2H phase. The electron-rich S increases the electron cloud density of Mo due to its strong electronegativity, which increases the shielding effect as a result. The Mo 3d peaks of 1T-Co-MoS_2 shift to lower binding energies of approximately 1 eV when compared with the peaks shown in 2H-MoS_2, and demonstrate a relaxation energy of 1 eV for the 1T phase derived from the 2H phase. The peaks at about 235.8 and 233.7 eV in the 1T-Co-MoS_2@HMCS are attributed to the existence of a small amount of Mo^{6+}. Deconvolution of the high-resolution spectrum in the Mo 3d region shows that the 1T phase content is as high as ~90%, indicating successful synthesis of 1T phase Co-MoS_2. Similarly, for the S 2p spectrum (Fig. 4c), the $2p_{1/2}$ and $2p_{3/2}$ peaks locate at 163.2 and 161.9 eV, which are approximately 1 eV lower than the corresponding binding energies of 2H-MoS_2 (164.3 and 162.6 eV). The changes in these peaks could be ascribed to the formation of 1T-MoS_2.[45] In addition, the low intensity of S 2s (Fig. 4b) in the 1T-Co-MoS_2@HMCS catalysts can be caused by the sulphur vacancy produced during the vapor-phase sulfidation process. The presence of sulphur vacancy leads to the destruction of Mo–S, which allows Mo to combine with oxygen to form MoO_3. That is why the peak intensity of Mo^{6+} of MoO_3 is slightly higher than that of Mo^{4+} of the 2H phase. Of course, leaving the sample in the air for a long time also increases the intensity of the Mo^{6+} peak.[13,46] Fig. S7b† shows the XPS spectrum in the Co 2p region. The spectrum is weaker than that of other elements, indicating relatively low contents of Co in the 1T-Co-MoS_2@HMCS, which agrees with the EDX mapping analysis results (Fig. 3h). The deconvoluted peaks at 794.0 and 779.1 eV could be assigned to the binding energy of $2p_{1/2}$ and $2p_{3/2}$ of Co^{3+}, respectively, whereas the peaks at 798.4 and 782.0 eV could be ascribed to the binding energy of $2p_{1/2}$ and $2p_{3/2}$ spin orbits of Co^{2+}. The peaks at 802.6 and 787.7 eV are the satellite peaks due to the surface complication.[47]

In order to exhibit the effectiveness of the multi-level space-confined strategy to obtain 1T-MoS_2, the XPS spectra and Raman spectra were further taken to demonstrate the contribution of each level of the strategy to the substable structure. As shown in the Mo 3d and S 2p XPS spectra presented in Fig. S8 and S9,† there is almost no 1T-MoS_2 in Co-MoS_2, and 1T-MoS_2 coexists with 2H-MoS_2 in Co-MoS_2@HMCS and MoS_2@HMCS. These results indicate that at each level, the strategy provides support to enhance the 1T-MoS_2 proportion. In particular, HMCS, with mesoporous structures capable of limiting nanosheet growth, play the most critical role, which is consistent with the Raman spectra (Fig. S10†).

Thus, all the above-mentioned results show that the 1T-Co-MoS_2@HMCS nanospheres synthesized by the spatial confinement strategy combined with vapor-phase sulfidation have been proven effective to obtain ultra-dispersed nano-sized 1T-Co-MoS_2 within the highly disordered mesoporous structure of HMCS. Hence, it is expected to obtain excellent electrocatalytic performance.

3.2 1T-Co-MoS_2@HMCS electrocatalytic performance evaluation for HER

To explore the HER electrocatalytic activity of the as-synthesized 1T-Co-MoS_2@HMCS, the electrochemical measurements of 1T-Co-MoS_2@HMCS were evaluated by linear sweep voltammetry (LSV) at a scan rate of 5 mV s^{-1} in 1 M KOH and 0.5 M H_2SO_4 aqueous solutions. As shown in Fig. 5, the HER performance of $(Co_2Mo_{10})(HM)_3$@HMCS, Co-MoS_2@HMCS, Co-MoS_2, HMCS and commercial 20% Pt/C was also investigated. Fig. 5a exhibits that 1T-Co-MoS_2@HMCS delivers smaller overpotentials (74 and 220 mV) compared with

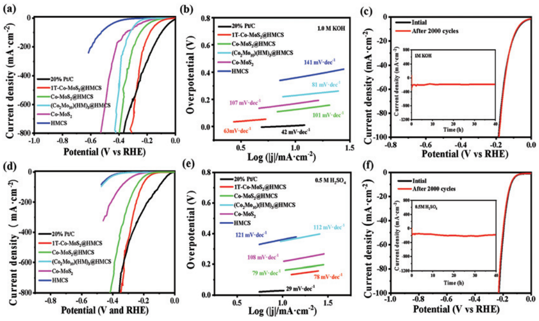

Fig. 5 (a) HER polarization curves of different electrodes and electrode materials in 1.0 M KOH. (b) Corresponding Tafel plots obtained from (a). (c) HER durability of 1T-Co-MoS_2@HMCS in 1.0 M KOH: polarization curves; the inset is the time dependence of catalytic currents. (d) HER polarization curves of different electrodes and electrode materials in 0.5 M H_2SO_4. (e) Corresponding Tafel plot obtained from (d). (f) HER durability of 1T-Co-MoS_2@HMCS in 0.5 M H_2SO_4: polarization curves; the inset is the time dependence of catalytic currents.

$(Co_2Mo_{10})(HM)_3$@HMCS (228 and 365 mV), Co-MoS_2@HMCS (123 and 295 mV), Co-MoS_2 (168 and 415 mV), and HMCS (358 and 595 mV) at −10 and −200 mA cm^{-2} in 1 M KOH, respectively. Among them, the HMCS shows the highest overpotential for HER in 1.0 M KOH, suggesting that the HMCS is inactive towards HER catalysis and only serves as a conductive substrate. Similarly, the LSV curve of $(Co_2Mo_{10})(HM)_3$@HMCS precursor also reflects inert hydrogen evolution activity. Compared with spatially confined 1T-Co-MoS_2 in HMCS, Co-MoS_2 without confinement exhibited low HER catalytic activity, indicating that the confinement of 1T-Co-MoS_2 within the mesoporous carbon sphere and the surfactants can significantly enhance the activity of catalytic materials. Besides, Co-MoS_2@HMCS shows reasonable HER catalytic activity, suggesting that the presence of HMCS itself without the surfactants can help disperse Co-MoS_2 to some extent. Thus, the above discussion for the LSV image results illustrates the positive effect of multi-level confinements. HER kinetics was further evaluated using Tafel plots. The Tafel slopes of 1T-Co-MoS_2@HMCS, $(Co_2Mo_{10})(HM)_3$@HMCS, Co-MoS_2@HMCS, Co-MoS_2, HMCS and commercial 20% Pt/C were calculated as 63, 81, 101, 107, 141 and 29 mV·dec^{-1} in 1 M KOH, respectively (Fig. 5b). The rather low Tafel slope of 1T-Co-MoS_2@HMCS suggests the fast rate of electron transfer kinetics. In addition, electrochemical impedance spectroscopic measurements were performed under acidic and alkaline conditions. As shown in Fig. S11,† the 1T-Co-MoS_2@HMCS electrocatalyst exhibits a much lower charge transfer resistance (R_{ct}) than a series of prepared CoMo catalysts, indicating the rapid interfacial reaction rate of the 1T-Co-MoS_2 catalyst in the HER process.[48]

Generally, the HER activity of catalysts is affected by the electrochemical active surface area (ECSA) and intrinsic activity; therefore, it is necessary to estimate the catalytically active surface area to reveal the effect of spatial confined regulation. The double-layer capacitance (C_{dl}) was investigated by cyclic voltammetry, which is generally proportional to the ECSA (Fig. S12 and S13†). 1T-Co-MoS_2@HMCS catalysts exhibited medium C_{dl}, suggesting that the improved HER activity of 1T-Co-MoS_2@HMCS catalysts originate from the enhanced intrinsic activity of each active site. Among them, C_{dl} of unconfined Co-MoS_2 proves the low electrochemical working area of undispersed Co_2Mo_{10}, implying a poor HER performance, which is consistent with the LSV results. C_{dl} test results show that Co_2Mo_{10} precursors, hexamethonium (HM) bromide surfactants, HMCS substrate, and vapor phase sulfidation all have a decisive contribution to the catalytic performance of the target catalyst. Stability was tested to reflect the durable operation of the electrocatalyst for water electrolysis. As shown in Fig. 5c, LSV curves before and after 20 000 cyclic voltammetry (CV) cycles were recorded to examine the stability in an alkaline medium, and the insert figure contains the *i-t* curve of 40 h at −200 mA cm^{-2} continuous electrolysis on 1T-Co-MoS_2@HMCS, which exhibits almost no deactivation for HER. The above-mentioned electrochemical tests have obtained similar results under acidic conditions. 1T-Co-MoS_2@HMCS exhibits superior low overpotential (132 and 245 mV at −10 and −200 mA·cm^{-2}, respectively), low Tafel slope (78 mV·dec^{-1}) and excellent cycle stability compared to other materials in 0.5 M H_2SO_4 (Fig. 5d–f). Table S1 and S2† list the detailed comparison of the HER performance of 1T-Co-MoS_2@HMCS with other reported recent non-precious electrocatalysts, revealing that the 1T-Co-MoS_2@HMCS nanosheet is superior to the reported Mo- or Co-based HER electrocatalysts.

In order to prove the benefits of POMs as a high-quality bimetal assembly platform, individual MoS_2@HMCS and CoS@HMCS, as well as their mechanically mixed nanostructures, were also prepared based on the related procedures reported in the literature, whose HER performances were evaluated by LSV, as shown in Fig. S14.† The nanospheres MoS_2@HMCS and CoS@HMCS both show inferior HER electrocatalytic activities, with potentials of 162 and 446 mV at −10 mA·cm^{-2} in 1 M KOH, respectively. The similar situation occurred in 0.5 M H_2SO_4, but MoS_2@HMCS had a reduced overpotential compared to that in alkaline solutions, implying a higher intrinsic activity of MoS_2 under acidic conditions, in agreement with previous studies.[16] In addition, 1T-Co-MoS_2@HMCS was also examined in neutral and sea water solutions, and showed reasonable performances (Fig. S15†).

The prominent HER performance of 1T-Co-MoS_2@HMCS could be ascribed to the following two reasons: (1) The multilevel confinement effect was shown to be an effective way to synthesize 1T-MoS_2 with abundant active sites, providing a structural basis for its high activity. Based on the advantageous platform of POMs, the dispersant improves the dispersion of active sites by inner-space-limited engineering. Meanwhile, the HMCS, as a nanoreactor with a large number of disordered mesoporous structures, was loaded with nanoscale MoS_2 sheets by outer-space-limited engineering. The diffusion length of molecules/ions was shortened, resulting in a large amount of H_2 production. (2) The bimetallic synergistic effect of 1T-MoS_2 was achieved by Co doping at the S-edge, which effectively adjusts the electronic structure and thus improves the absorption and desorption efficiency of H_2.

3.3 DFT calculations

We developed a 1T-Co-MoS_2 model for DFT calculations and investigated the doping effect on the HER activity of 1T-MoS_2 by substituting different Mo sites with Co (Fig. S16†). The adsorption model for acidic and alkaline conditions is shown in Fig. S17 and S18.† As shown in Fig. 6a, we discuss the contribution of different types of S sites to the catalytic activity. Fig. 6b reports the energy barriers of H_2O dissociation and H_2 desorption in an alkali environment. The H_2O dissociation step is the rate-limiting step, and the free energy barrier follows the trend of Mo–S basal sites (2.29 eV) > Co–S basal site (2.21 eV) > Mo–S edge site (2.07 eV) > Co–S edge site (1.94 eV). For the desorption process of H_2, ΔG_{H^*} on the Co–S edge site (1.14 eV) is much lower than that on the Mo–S basal site of 1T MoS_2 (1.60 eV), the Co–S basal site (1.50 eV), and the Mo–S edge site (1.34 eV) of 1T-Co-MoS_2, demonstrating the easier desorption process on Co–S edge sites. These calculations are consistent with the experimental finding that the most active site of 1T-Co-MoS_2@HMCS is the Co–S edge site, lowering the free energy for H_2O dissociation and H desorption, both important steps in alkaline HER, giving rise to enhanced activity towards HER and reflecting the major significance of Co doping.[49,50] Moreover, the DFT calculation results exhibited a similar activity trend under acidic solutions (Fig. 6c), indicating the high intrinsic activity of the Co–S edge sites. The calculated results are in agreement with the results of previous studies, which confirmed that the Heyrovsky route for the complete HER pathway is more favourable than the Tafel route.[14]

The atomic interaction of 1T-MoS_2 and Co was further studied based on the electronic structure analysis. Due to the doping effects of Co, the S atoms are more positively charged than pure 1T-MoS_2, thus forming a built-in electric field, so that the charges can be quickly transferred between Co and S (Fig. S19†). Compared with the Mo–S basal site of 1T-MoS_2 and the Co–S basal site of 1T-Co-MoS_2 (cobalt doped inside), the DOS of the Co–S edge site near the Fermi level enhanced (Fig. S20†), indicating that the synergetic effects of Co and S in the boundary significantly increased the charge transfer during water splitting.[51] Furthermore, the d-band centre of S atoms in the Co edge site of 1T-Co-MoS_2 system is also shifted to a higher energy of −0.752 eV than that in the 1T-MoS_2 system (−1.162 eV) and Co basal site of 1T-Co-MoS_2 (−1.025 eV) (Fig. S20†). The shift of the d-band centre would further lead to less occupation of the antibonding states between the Co edge of 1T-Co-MoS_2 and adsorbed intermediates, thereby enhancing their binding strength. The DOS and PDOS results show the positive roles of the synergetic coupling effects of Co and S in the boundary, confirming that the density of the unoccupied e_g orbit state increased in the Co edge of 1T-Co-MoS_2 (Fig. S21†). With enhanced conductivity, improved binding strength with intermediates and unoccupied e_g orbits, the Co–S edge site of 1T-Co-MoS_2 can significantly optimize the HER activity.

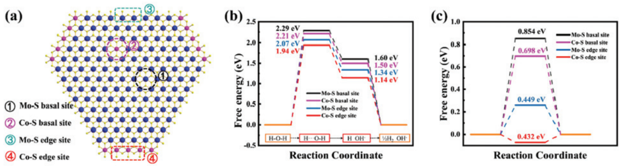

Fig. 6 (a) Schematic diagram of the atomic model and sites. Free energies of hydrogen atom adsorption on the basal plane of pristine 1T-MoS_2 as well as on the Mo–S edge and Co–S edge of 1T-Co-MoS_2@HMCS in alkaline (b) and acidic solutions (c).

3.4 Structure–activity relationship

As shown in Fig. 7, the optimized combination of Co_2Mo_{10} binary POMs, hexamethonium (HM) bromide surfactants, and HMCS substrates shows obvious synergistic effects for the design and synthesis of efficient HER catalysts. Consequently, the well-dispersed (1–3 layers), ultrafine (<5 nm), and metastable Co-doped 1T-MoS_2 nanoclusters were *in situ* fabricated from the POM-based molecular precursor *via* a multi-level spatial confinement strategy. Based on the aforementioned experimental results, we conclude three advantages for the superior precursors $(Co_2Mo_{10})(HM)_3$@HMCS and the corresponding multi-level spatial confinement strategy, so-called “killing three birds with one stone”, as follows: First, the nanosized Co_2Mo_{10} molecules with a strong and intimate Co–O–Mo interaction facilitated the formation of the Co-promoted MoS_2 phase, that is so-called Co-MoS_2 active sites. The Mo atom at the S-edge in MoS_2 is preferential substituted by Co to generate new Co–S edges, leading to the shape transformation from triangular MoS_2 to truncated triangular Co-MoS_2 clusters. This result was verified by considering a previously reported study.[40] Second, the cationic surfactant hexamethonium (HM) bromide was used for dispersing the Co-MoS_2 nanosheets and preventing them from stacking in the [002] direction, resulting in the formation of single- or few-layer Co-MoS_2 protected by organic buffer layers. As the previous studies suggested, the expanded interlayer spacing of MoS_2 can be beneficial for the formation of 1T-MoS_2.[52] However, ultra-small Co-MoS_2 nanosheets often suffer from severe aggregation and poor thermal stability for their high surface free energy. Third, mesoporous HMCS were therefore adopted to greatly stabilize single-layer nanoclusters and inhibit the epitaxial growth of

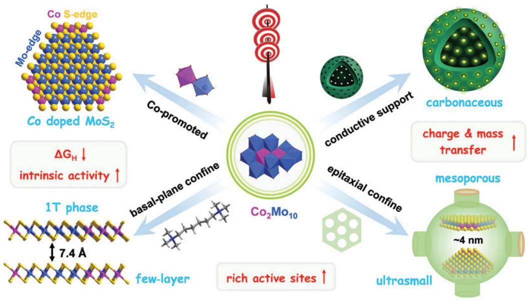

Fig. 7 Schematic diagram of the design and fabrication of the 1T-Co-MoS_2@HMCS catalyst from the POM-based precursor $(Co_2Mo_{10})(HM)_3$@HMCS *via* a multi-level spatial confined strategy.

MoS_2, favouring the formation of metastable 1T-MoS_2 in the confined spaces.

In addition, 1T-Co-MoS_2@HMCS not only preserves the mesoporous structure to expose rich Co-MoS_2 edge active sites in a network of pores, but also acts as an effective electron conductor, electrolyte transporter and active site protector to enhance charge and mass transfer, which can effectively confine the catalytic HER in hollow sphere structures and make each mesopore configuration as an independent and efficient HER active ecosystem.[53] Therefore, the great HER electrocatalytic performance of 1T-Co-MoS_2@HMCS should be attributed to its unique structure, high intrinsic activity from Co-doped 1T-MoS_2 sites, abundant exposed active sites from ultra-dispersed nanosheets, and enhanced charge and mass transfer within the HMCS substrate.

4. Conclusions

In summary, highly dispersed 1T-Co-MoS_2 nanoclusters with few layers and ultra-small size have been successfully fabricated and encapsulated within HMCS conductive substrates by spatially confining engineering. During *in situ* vapor-phase sulfurization, the optimized precursor combination of Co_2Mo_{10} binary POMs, hexamethonium (HM) bromide surfactants, and HMCS substrates exhibits synergistically confined growth effects from the atomic level, molecular level to mesoscopic scale, thereby achieving the simultaneous regulation of active sites, basal planes, and epitaxial growth of MoS_2. When evaluated as an electrocatalyst for the HER process, 1T-Co-MoS_2@HMCS shows a prominent activity and excellent long-term durability, and only requires an overpotential of 220 and 245 mV at 200 mA cm^{-2} current density in 1 M KOH and 0.5 M H_2SO_4 electrolytes, respectively. DFT calculations further reveal that Co–S edge sites possess highly intrinsic activity in Co-doped 1T-MoS_2 for HER, reflecting the major significance of Co doping. Meanwhile, the mesoporous and carbonaceous structures of HMCS can expose the numerous Co-doped 1T-MoS_2 active edge sites and promote faster charge and mass transfer to enhance the apparent catalytic activity. Thus, this work provides the first facile preparation of high-purity Co-doped 1T-MoS_2 by multi-level spatial confinement and offers an effective way to solve the poor basic activity through Co doping, which offers a reasonable scheme for the design and synthesis of other metastable nanomaterials derived from POM-based hybrid precursors.

Conflicts of interest

There are no conflicts to declare

Acknowledgements

This work is financially supported by the National Natural Science Foundation of China (21878336, 21805308), the Shandong Provincial Natural Science Foundation, China (ZR2018MB035), the Key Research and Development Project of Shandong Province (2019GSF109075), the Fundamental Research Funds for the Central Universities (20CX02213A), and the China University of Petroleum, Huadong (YCX2021153).

References

1 M. Li, B. Cai, R. Tian, X. Yu, M. B. H. Breese, X. Chu, Z. Han, S. Li, R. Joshi, A. Vinu, T. Wan, Z. Ao, J. Yi and D. Chu, Vanadium doped 1T MoS2 nanosheets for highly efficient electrocatalytic hydrogen evolution in both acidic and alkaline solutions, *Chem. Eng. J*, 2021, **409**, 128158.

2 Z. W. Seh, J. Kibsgaard, C. F. Dickens, I. Chorkendorff, J. K. Nørskov and T. F. Jaramillo, Combining theory and experiment in electrocatalysis: Insights into materials design, *Science*, 2017, **355**, eaad4998.

3 C. C. McCrory, S. Jung, I. M. Ferrer, S. M. Chatman, J. C. Peters and T. F. Jaramillo, Benchmarking hydrogen evolving reaction and oxygen evolving reaction electrocatalysts for solar water splitting devices, *J. Am. Chem. Soc.*, 2015, **137**, 4347–4357.

4 J. Yang, J. K. Cooper, F. M. Toma, K. A. Walczak, M. Favaro, J. W. Beeman, L. H. Hess, C. Wang, C. Zhu, S. Gul, J. Yano, C. Kisielowski, A. Schwartzberg and I. D. Sharp, A multifunctional biphasic water splitting catalyst tailored for integration with high-performance semiconductor photoanodes, *Nat. Mater.*, 2017, **16**, 335–341.

5 Z. H. Xue, H. Su, Q. Y. Yu, B. Zhang, H. H. Wang, X. H. Li and J. S. Chen, Janus Co/CoP Nanoparticles as Efficient Mott–Schottky Electrocatalysts for Overall Water Splitting in Wide pH Range, *Adv. Energy Mater.*, 2017, **7**, 1602355.

6 C. Chen, A. Wu, H. Yan, Y. Xiao, C. Tian and H. Fu, Trapping $[PMo_{12}O_{40}]^{3-}$ clusters into pre-synthesized ZIF-67 toward Mo_xCo_xC particles confined in uniform carbon polyhedrons for efficient overall water splitting, *Chem. Sci.*, 2018, **9**, 4746–4755.

7 Y. J. Tang, Y. Wang, X. L. Wang, S. L. Li, W. Huang, L. Z. Dong, C. H. Liu, Y. F. Li and Y. Q. Lan, Molybdenum Disulfide/Nitrogen-Doped Reduced Graphene Oxide Nanocomposite with Enlarged Interlayer Spacing for Electrocatalytic Hydrogen Evolution, *Adv. Energy Mater.*, 2016, **6**, 1600116.

8 J. Hou, B. Zhang, Z. Li, S. Cao, Y. Sun, Y. Wu, Z. Gao and L. Sun, Vertically Aligned Oxygenated-CoS_2–MoS_2 Heteronanosheet Architecture from Polyoxometalate for Efficient and Stable Overall Water Splitting, *ACS Catal.*, 2018, **8**, 4612–4621.

9 J. D. Benck, T. R. Hellstern, J. Kibsgaard, P. Chakthranont and T. F. Jaramillo, Catalyzing the Hydrogen Evolution Reaction (HER) with Molybdenum Sulfide Nanomaterials, *ACS Catal.*, 2014, **4**, 3957–3971.

10 H. I. Karunadasa, E. Montalvo, Y. Sun, M. Majda, J. R. Long and C. J. Chang, A Molecular MoS_2 Edge Site Mimic for

Catalytic Hydrogen Generation, *Science*, 2012, **335**, 698–702.

11 J. Zhang, J. Wu, H. Guo, W. Chen, J. Yuan, U. Martinez, G. Gupta, A. Mohite, P. M. Ajayan and J. Lou, Unveiling Active Sites for the Hydrogen Evolution Reaction on Monolayer MoS2, *Adv. Mater.*, 2017, **29**, 1701955.

12 Z. Lei, J. Zhan, L. Tang, Y. Zhang and Y. Wang, Recent Development of Metallic (1T) Phase of Molybdenum Disulfide for Energy Conversion and Storage, *Adv. Energy Mater.*, 2018, **8**, 1703482.

13 Y. Huang, Y. Sun, X. Zheng, T. Aoki, B. Pattengale, J. Huang, X. He, W. Bian, S. Younan, N. Williams, J. Hu, J. Ge, N. Pu, X. Yan, X. Pan, L. Zhang, Y. Wei and J. Gu, Atomically engineering activation sites onto metallic 1T-MoS2 catalysts for enhanced electrochemical hydrogen evolution, *Nat. Commun.*, 2019, **10**, 982.

14 Q. Tang and D. E. Jiang, Stabilization and Band-Gap Tuning of the 1T-MoS_2 Monolayer by Covalent Functionalization, *Chem. Mater.*, 2015, **27**, 3743–3748.

15 Z. Zhu, H. Yin, C. T. He, M. Al-Mamun, P. Liu, L. Jiang, Y. Zhao, Y. Wang, H. G. Yang, Z. Tang, D. Wang, X. M. Chen and H. Zhao, Ultrathin Transition Metal Dichalcogenide/3d Metal Hydroxide Hybridized Nanosheets to Enhance Hydrogen Evolution Activity, *Adv. Mater.*, 2018, **30**, 1801171.

16 D. Cao, K. Ye, O. A. Moses, W. Xu, D. Liu, P. Song, C. Wu, C. Wang, S. Ding, S. Chen, B. Ge, J. Jiang and L. Song, Engineering the In-Plane Structure of Metallic Phase Molybdenum Disulfide via Co and O Dopants toward Efficient Alkaline Hydrogen Evolution, *ACS Nano*, 2019, **13**, 11733–11740.

17 R. Forsythe, C. Cox, M. Wilsey and A. Müller, Pulsed Laser in Liquids Made Nanomaterials for Catalysis, *Chem. Rev.*, 2021, **121**, 7568–7637.

18 J. Guo, X. Zhang, Y. Sun, L. Tang and X. Zhang, Self-template Synthesis of Hierarchical $CoMoS_3$ Nanotubes Constructed of Ultrathin Nanosheets for Robust Water Electrolysis, *J. Mater. Chem. A*, 2017, **5**, 11309–11315.

19 S. S. Grønborg, N. Salazar, A. Bruix, J. Rodríguez-Fernández, S. D. Thomsen, B. Hammer and J. V. Lauritsen, Visualizing Hydrogen-induced Reshaping and Edge Activation in MoS2 and Co-promoted MoS2 Catalyst Clusters, *Nat. Commun.*, 2018, **9**, 2211.

20 N. H. Attanayake, A. C. Thenuwara, A. Patra, Y. V. Aulin, T. M. Tran, H. Chakraborty, E. Borguet, M. L. Klein, J. P. Perdew and D. R. Strongin, Effect of Intercalated Metals on the Electrocatalytic Activity of 1T-MoS_2 for the Hydrogen Evolution Reaction, *ACS Energy Lett.*, 2018, **3**, 7–13.

21 J. Strachan, A. F. Masters and T. Maschmeyer, Critical review: hydrothermal synthesis of 1T-MoS_2 – an important route to a promising material, *J. Mater. Chem. A*, 2021, **9**, 9451–9461.

22 K. Chang, X. Hai, H. Pang, H. Zhang, L. Shi, G. Liu, H. Liu, G. Zhao, M. Li and J. Ye, Targeted Synthesis of 2H- and 1T-Phase MoS_2 Monolayers for Catalytic Hydrogen Evolution, *Adv. Mater.*, 2016, **28**, 10033–10041.

23 X. Chen, Z. Wang, Y. Wei, X. Zhang, Q. Zhang, L. Gu, L. Zhang, N. Yang and R. Yu, High Phase-Purity 1T-MoS_2 Ultrathin Nanosheets by a Spatially Confined Template, *Angew. Chem., Int. Ed.*, 2019, **58**, 17621–17624.

24 Y. Jiao, W. Hong, P. Li, L. Wang and G. Chen, Metal-organic framework derived Ni/NiO micro-particles with subtle lattice distortions for high-performance electrocatalyst and supercapacitor, *Appl. Catal., B*, 2019, **244**, 732–739.

25 Y. K. Lu, C. L. Yue, Y. P. Li, W. J. Bao, X. X. Guo, W. F. Yang, Z. Liu, P. Jiang, W. Yan, S. Liu, Y. Pan and Y. Q. Liu, Atomically dispersed Ni on Mo2C embedded in N, P co-doped carbon derived from polyoxometalate supramolecule for high-efficiency hydrogen evolution electrocatalysis, *Appl. Catal., B*, 2021, **296**, 120336.

26 Y. Y. Ma, C. X. Wu, X. J. Feng, H. Q. Tan, L. K. Yan, Y. Liu, Z. H. Kang, E. B. Wang and Y. G. Li, Highly efficient hydrogen evolution from seawater by a low-cost and stable CoMoP@C electrocatalyst superior to Pt/C, *Energy Environ. Sci.*, 2017, **10**, 788–798.

27 B. Huang, D. H. Yang and B. H. Han, Application of polyoxometalate derivatives in rechargeable batteries, *J. Mater. Chem. A*, 2020, **8**, 4593–4628.

28 Y. K. Lu, X. X. Guo, L. Y. Yang, W. F. Yang, W. Sun, Y. Tuo, Y. Zhou, S. Wang, Y. Pan, W. Yan, D. Sun and Y. Liu, Highly efficient CoMoS heterostructure derived from vertically anchored Co5Mo10 polyoxometalate for electrocatalytic overall water splitting, *Chem. Eng. J.*, 2020, **394**, 124849.

29 J. S. Li, Y. Wang, C. H. Liu, S. L. Li, Y. G. Wang, L. Z. Dong, Z. H. Dai, Y. F. Li and Y. Q. Lan, Coupled molybdenum carbide and reduced graphene oxide electrocatalysts for efficient hydrogen evolution, *Nat. Commun.*, 2016, **7**, 11204.

30 J. A. Toledo-Antonio, M. A. Cortes-Jacome, J. Escobar-Aguilar, C. Angeles-Chavez, J. Navarrete-Bolaños and E. López-Salinas, Upgrading HDS activity of MoS_2 catalysts by chelating thioglycolic acid to MoO_x supported on alumina, *Appl. Catal., B*, 2017, **213**, 106–117.

31 Z. Li, X. Zhang, H. Cheng, J. Liu, M. Shao, M. Wei, D. G. Evans, H. Zhang and X. Duan, Confined Synthesis of 2D Nanostructured Materials toward Electrocatalysis, *Adv. Energy Mater.*, 2020, **10**, 1900486.

32 S. Li, A. Pasc, V. Fierro and A. Celzard, Hollow carbon spheres, synthesis and applications – a review, *J. Mater. Chem. A*, 2016, **4**, 12686–12713.

33 Z. Yu, N. Ji, J. Xiong, X. Li, R. Zhang, L. Zhang and X. Lu, Ruthenium-Nanoparticle-Loaded Hollow Carbon Spheres as Nanoreactors for Hydrogenation of Levulinic Acid: Explicitly Recognizing the Void-Confinement Effect, *Angew. Chem., Int. Ed.*, 2021, **60**, 20786–20794.

34 G. Prieto, H. Tüysüz, N. Duyckaerts, J. Knossalla, G. H. Wang and F. Schüth, Hollow Nano- and Microstructures as Catalysts, *Chem. Rev.*, 2016, **116**, 14056–14119.

35 A. Misra, K. Kozma, C. Streb and M. Nyman, Beyond Charge Balance: Counter-Cations in Polyoxometalate Chemistry, *Angew. Chem., Int. Ed.*, 2020, **59**, 596–612.

36 J. V. Lauritsen, J. Kibsgaard, G. H. Olesen, P. G. Moses, B. Hinnemann, S. Helveg, J. K. Nørskov, B. S. Clausen, H. Topsøe, E. Lægsgaard and F. Besenbacher, Location and coordination of promoter atoms in Co- and Ni-promoted MoS_2-based hydrotreating catalysts, *J. Catal.*, 2007, **249**, 220–233.

37 J. V. Lauritsen and F. Besenbacher, Atom-resolved scanning tunneling microscopy investigations of molecular adsorption on MoS_2 and CoMoS hydrodesulfurization catalysts, *J. Catal.*, 2015, **328**, 49–58.

38 A. S. Walton, J. V. Lauritsen, H. Topsøe and F. Besenbacher, *J. Catal.*, 2013, **308**, 306–318.

39 N. K. Perkgoz and M. Bay, Investigation of Single-Wall MoS_2 Monolayer Flakes Grown by Chemical Vapor Deposition, *Nano-Micro Lett.*, 2016, **8**, 70–79.

40 S. Li, S. Wang, T. Xu, H. Zhang, Y. Tang, S. Liu, T. Jiang, S. Zhou and H. Cheng, Growth mechanism and atomic structure of group-IIA compound-promoted CVD-synthesized monolayer transition metal dichalcogenides, *Nanoscale*, 2021, **13**, 13030–13041.

41 P. K. Sahoo, S. Memaran, Y. Xin, L. Balicas and H. R. Gutiérrez, One-pot growth of two-dimensional lateral heterostructures via sequential edge-epitaxy, *Nature*, 2018, **553**, 63–67.

42 J. Staszak-Jirkovský, C. D. Malliakas, P. P. Lopes, N. Danilovic, S. S. Kota, K. C. Chang, B. Genorio, D. Strmcnik, V. R. Stamenkovic, M. G. Kanatzidis and N. M. Markovic, Design of active and stable Co-Mo-Sx chalcogels as pH-universal catalysts for the hydrogen evolution reaction, *Nat. Mater.*, 2016, **15**, 197–203.

43 T. An, Y. Wang, J. Tang, W. Wei, X. Cui, A. M. Alenizi, L. Zhang and G. Zheng, Interlaced NiS_2-MoS_2 nanoflake-nanowires as efficient hydrogen evolution electrocatalysts in basic solutions, *J. Mater. Chem. A*, 2016, **4**, 13439–13443.

44 G. Eda, H. Yamaguchi, D. Voiry, T. Fujita, M. Chen and M. Chhowalla, Photoluminescence from Chemically Exfoliated MoS_2, *Nano Lett.*, 2011, **11**, 5111–5116.

45 W. Zhou, Z. Yin, Y. Du, X. Huang, Z. Zeng, Z. Fan, H. Liu, J. Wang and H. Zhang, Synthesis of Few-Layer MoS_2 Nanosheet-Coated TiO_2 Nanobelt Heterostructures for Enhanced Photocatalytic Activities, *Small*, 2013, **9**, 140–147.

46 X. Y. Yu, Y. Feng, Y. Jeon, B. Guan, X. W. Lou and U. Paik, Formation of Ni–Co–MoS_2 Nanoboxes with Enhanced Electrocatalytic Activity for Hydrogen Evolution, *Adv. Mater.*, 2016, **28**, 9006–9011.

47 Y. Yang, H. Yao, Z. Yu, S. M. Islam, H. He, M. Yuan, Y. Yue, K. Xu, W. Hao, G. Sun, H. Li, S. Ma, P. Zapol and M. G. Kanatzidis, Hierarchical Nanoassembly of MoS_2/Co_9S_8/Ni_3S_2/Ni as a Highly Efficient Electrocatalyst for Overall Water Splitting in a Wide pH Range, *J. Am. Chem. Soc.*, 2019, **141**, 10417–10430.

48 P. Zhou, C. Wang, Y. Liu, Z. Wang, P. Wang, X. Qin, X. Zhang, Y. Dai, M. H. Whangbo and B. Huang, Sulfuration of NiV-layered double hydroxide towards novel supercapacitor electrode with enhanced performance, *Chem. Eng. J.*, 2018, **351**, 119–126.

49 J. Liang, C. Ding, J. Liu, T. Chen, W. Peng, Y. Li, F. Zhang and X. Fan, Heterostructure engineering of Co-doped MoS_2 coupled with Mo_2CTx MXene for enhanced hydrogen evolution in alkaline media, *Nanoscale*, 2019, **11**, 10992–11000.

50 F. Ma, Y. Liang, P. Zhou, F. Tong, Z. Wang, P. Wang, Y. Liu, Y. Dai, Z. Zheng and B. Huang, One-step synthesis of Co-doped 1T-MoS2 nanosheets with efficient and stable HER activity in alkaline solutions, *Mater. Chem. Phys.*, 2020, **244**, 122642.

51 Y. Zheng, Y. Jiao, A. Vasileff and S. Z. Qiao, The Hydrogen Evolution Reaction in Alkaline Solution: From Theory, Single Crystal Models, to Practical Electrocatalysts, *Angew. Chem., Int. Ed.*, 2018, **57**, 7568–7579.

52 Z. Wang, T. Chen, W. Chen, K. Chang, L. Ma, G. Huang, D. Chen and J. Y. Lee, CTAB-assisted synthesis of single-layer MoS_2–graphene composites as anode materials of Li-ion batteries, *J. Mater. Chem. A*, 2013, **1**, 2202–2210.

53 B. Wang, Y. Ye, L. Xu, Y. Quan, W. Wei, W. Zhu, H. Li and J. Xia, Space-Confined Yolk-Shell Construction of Fe3O4 Nanoparticles Inside N-Doped Hollow Mesoporous Carbon Spheres as Bifunctional Electrocatalysts for Long-Term Rechargeable Zinc–Air Batteries, *Adv. Funct. Mater.*, 2020, **30**, 2005834.